Thermal Response of an Orthotropic Non-charring Ablative Material

Massoud Tatar[1]

Abstract

In this paper, the thermal response of orthotropic carbon–carbon is studied. In the first step, non-charring materials ablation is implemented into a finite volume solver. Carbon–carbon ablative thermal behavior is studied under a time-dependent heat flux. The equilibrium surface thermochemistry model of carbon ablation in air including the diffusion and sublimation along with energy source term, heated wall recession and material properties are all applied in FLUENT 6.3 solver via user-defined functions. Stagnation point temperature, recession and net heat flux for the isotropic case are compared with the published one-dimensional finite difference results. Subsequently, the effects of orthotropic conductivity of the material on surface temperature, ablation mass flux, recession rate of the heated wall and the temperature distribution through the material are described. Results indicate that higher surface temperature and ablation mass flux as well as lower interior temperatures are achieved by the orthotropic material response, compared to the isotropic one. The same conclusion can be made by increasing the ratio of "in-plane" to "through-the-thickness" conductivities. In brief, this work presents a methodology for modeling two- and three-dimensional non-charring material ablation within FLUENT solver to study the thermal response of an anisotropic ablator, sharp geometries and metal–insulator interface where a classic one-dimensional approach is inaccurate.

List of Symbols

ρ	Density (kg/m^3)
C_p	Specific heat (J/kg K)
T	Temperature (K)
k	Conductivity (W/mK)
h_w	Wall enthalpy at vapor side (J/kg)
h_u	Wall enthalpy at underside (J/kg)
T_{ref}	Reference temperature (K)
$\dot{m}_{eq}$	Equilibrium mass flux $(kg/m^2\ s)$
q_{cw}	Cold wall heat flux (W/m^2)
q_{conv}	Convective heat flux (W/m^2)
q_r	Radiative heat flux (W/m^2)
q_{ab}	Ablative heat flux (W/m^2)
$\dot{m}_{ab}$	Ablation mass flux $(kg/m^2\ s)$
$\dot{m}_R$	Rate-controlled oxidation mass flux $(kg/m^2\ s)$
P^*	Normalized freestream pressure
$\dot{S}_w$	Wall recession rate (m/s)
h_r	Recovery enthalpy (J/kg)
g_h	Convective heat transfer $(W/m^2\ K)$
g_{ho}	Convective heat transfer without injection $(W/m^2\ K)$
φ_{Blow}	Blowing factor
φ_{Hal}	Heating augmentation level
ε	Emissivity
σ	Stefan–Boltzmann $(5.67 \times 10^{-8}\ W/m^2\ K^4)$
R_n	Nose radius (m)
u_∞	Freestream velocity (m/s)
X_{O_2}	Mole fraction of oxygen in air

✉ Massoud Tatar
massoudtatar@ut.ac.ir

1 Faculty of New Sciences and Technologies, University
of Tehran, Tehran, Iran

1 Introduction

The tolerance of great amount of heat by a structure is always a design challenge. The correct evaluation of thermo-mechanical exerted loads on the underlying structures is necessary for a successful space mission. Blunt nose of hypersonic vehicles experiences high temperature and pressure due to strong shock wave and is exposed to very high levels of mechanical stress during atmospheric entry. Throat part of the solid rocket nozzles is also subjected to severe temperature gradients which may cause structural failure. Therefore, it is essential to apply engineering techniques to protect structures from high heat loads. Among the various

existing approaches, carbon-based ablative heat shields are of the most favorite materials used to minimize the heat conducted into the body. The mass removal from the heated surface during ablation process leads to the energy rejection into the boundary layer and in consequence lower wall heating. This phenomenon may take place by phase change, chemical erosion, oxidation and mechanical removal mechanisms. Comparing charring and non-charring carbon-based materials, the latter are less effective in heat flux reduction to substructures because of their higher thermal conductivity. Nevertheless, they are commonly used in regions subjected to large shear stresses and pressure gradients because of their higher density in comparison with charring heat shields. Designing an efficient thermal protection system (TPS) is always of great concern to aerospace engineers. For this reason, vast numerical and experimental studies have been carried out over the ablative materials. Mastanaiah [1] correlated the theoretical analysis with the experimental data obtained for surface recession, char depth and temperatures in silica phenolic and carbon phenolic ablators from static test conducted on rocket nozzles and found a strong dependence of effective thermal conductivity of char on the wall heat flux. Blackwell [2] adapted the exponential differencing scheme of Spalding to solve one-dimensional ablation problems by using a grid attached to the receding surface using the finite volume approach. Detailed description of one-dimensional thermal response of carbon–carbon and carbon–phenolic materials using finite difference technique, and heat balance integral methods are described in [3, 4]. A quasi-one-dimensional ablation analysis for a sharp-nosed, reusable, reentry vehicle using an in-house code with the aero-thermodynamic results computed by FLUENT 6.2 was conducted by Candane et al. [5]. Chen et al. [6, 7] presented an integral thermal pyrolysis model for the transient pyrolysis of charring and non-charring materials. They also suggested a methodology for deriving material pyrolysis properties and validated it by utilizing three charring materials. An improved lumped differential approach for ablative thermal protection analysis including the use of materials with low thermal diffusivity was proposed by Ruperti et al. [8]. Amar [9] developed and verified a one-dimensional finite volume code to calculate ablation response with porous flow. Candane et al. [10] conducted a coupling between the heat flux of a hypersonic laminar flow solver with an ablation quasi-one-dimensional code for spherical and cylindrical geometries. The governing differential equations for ablative thermal response in three dimensions using the finite element method employing Darcy law to model the flow of pyrolysis gas were solved by Dec [11]. Arnas et al. [12] described the problem of aerodynamic heat transfer in a complete analytical form for better understanding and correct use in the design of TPS. An analytical solution of the ablation of a two-layer composite is found in [13], which

includes an ablative layer and a non-ablative substrate, subjected to a Gaussian heat flux. Ewing et al. [14] developed a numerical method for solving one-dimensional ablation heat transfer problems with control volume technique. A material response code coupled with surface ablation and pyrolysis to a hypersonic solver for weakly ionized flows in thermochemical non-equilibrium was presented by Martin, Boyd [15]. They proposed a blowing boundary condition for the flow field solver which allows the ablating gas calculated by the material response code to be correctly injected into the boundary layer. Chen et al. [16] performed transient simulations to predict in-depth thermal response and surface recession of phenolic-impregnated carbon ablator (PICA) using a finite volume material response code using CEA results to account for the ablation process. A physical and mathematical model for a diffusion-controlled Stefan problem with finite rate chemical reaction at moving boundary for a graphite heat shield plate withstanding aerodynamic heating was proposed by Qu et al. [17]. The transient regime behavior of a three-dimensional carbon–carbon composite, where the response of surface roughness evolution and the effective reactivity were computed, was investigated by Lachaud et al. [18]. A thermochemical ablation model of carbon–carbon composite, based on the lattice Boltzmann method considering the flow, diffusion, chemical reaction, heat transfer and the evolution of solid phase, was established by Wang, Zhu [19]. Zong et al. [20] experimentally investigated the pyrolysis of non-charring acrylonitrile butadiene styrene (ABS) in a reduced pressure chamber under different external heat fluxes. A one-dimensional numerical model was developed to predict the top surface and the bottom surface temperatures of ABS during the pyrolysis. Wang et al. [21] developed a transient, one-dimensional numerical model to describe the processes of transpiration cooling and ablation of the porous matrix used for the cooling. The model was based on the assumption of local thermal equilibrium. Qian et al. [22] proposed a heat flux estimation algorithm using the conjugate gradient optimization method and utilized one-dimensional finite control volume method to validate the effectiveness of the algorithm.

Although a significant amount of research has been done on the numerical study of the ablation process, as briefly described in the literature, most of it considers a one-dimensional approach to deal with the ablation phenomenon which limits the application in industrial problems. Sharp geometries such as the leading edge of a fin, high temperature flows with a nonzero angle of attack over a blunt body, orthotropic or anisotropic materials heat conduction and the conduction through an interface between ablative and metallic materials are all the examples where the physics of the problem violates from one-dimensional assumption, and the predictions based on this hypothesis are unreliable. In this work, multidimensional investigation of non-charring ablative

materials is provided. Implementation of carbon–carbon material thermal behavior in FLUENT 6.3 is performed. The EST model of carbon ablation in air including the diffusion and sublimation, the energy equation source term, temperature-dependent boundary condition, temperature-dependent material properties and the heated wall recession are all considered in modeling via user-defined functions (UDF) written in C programming language. Code-to-code validation is performed with the published results of one-dimensional finite difference and hybrid balance integral (HBI) methods at stagnation point. Subsequently, the effects of orthotropic conductivity on thermal response of the ablator are discussed. Within the framework of a fast multidimensional ablation solver, it is possible to investigate the thermal behavior of an arbitrary geometry such as leading edges or anisotropic materials, where a one-dimensional material response approximation fails. This capability also provides temperature field distribution which can be used further to compute the thermal stresses in the material via multiphysics simulations.

2 Governing Equations

Considering the assumption of thermal equilibrium at the heated surface of a two-dimensional non-charring ablator, the energy equation in solid material including the effects of material anisotropy leads to a single energy equation:

$$\frac{\partial (\rho C_P T)}{\partial t}\bigg|_{x,y} = k\frac{\partial^2 T}{\partial x^2} + k\frac{\partial^2 T}{\partial y^2} + \frac{\partial k}{\partial x}\frac{\partial T}{\partial x} + \frac{\partial k}{\partial y}\frac{\partial T}{\partial y} \quad (1)$$

The surface energy balance equation yields to the following preferred form for non-charring ablator. Sorting this equation results in the amount of conductive heat transfer at the heated surface.

$$\dot{q}_{conv} - \dot{q}_r - \dot{q}_{ab} - \dot{q}_{cond} = 0 \quad (2)$$

Under a unity Lewis number assumption, convective heat flux becomes proportional to the difference between the recovery and heated wall enthalpies as follows:

$$\dot{q}_{conv} = g_h(h_r - h_w) \quad (3)$$

The parameter, g_h, is the heat transfer coefficient in the presence of ablation and is correlated with blowing factor and erosion effect and is given by:

$$g_h = g_{ho} \cdot \varphi_{blow} \cdot \varphi_{hal} \quad (4)$$

The effects of surface reactions of carbon injected into the boundary layer are taken into account via blowing factor $(\varphi_{blow} \leq 1)$ and are defined by:

$$\varphi_{blow} = \frac{a B_0}{\exp(a B_0) - 1} \quad (5)$$

where a is the blowing coefficient and varies generally with injected gas species and flow conditions such as stagnation point, laminar or turbulent regime of flow and Mach number. Here, it is assumed to be equal to 1.5 for carbon–carbon based on Putz, Bartlett [23].

The ratio between ablation mass flux and convective heat transfer coefficient in the absence of surface ablation is denoted by B_0 as follows:

$$B_0 = \frac{\dot{m}_{ab}}{g_{h0}} \quad (6)$$

For the sake of simplicity, a unity value is employed for the heating augmentation level ($\varphi_{hal} \geq 1$) throughout this study.

The net heat flux radiated from heated surface to the surrounding environment is given by:

$$\dot{q}_r = \varepsilon\sigma\left(T_w^4 - T_{ref}^4\right) \quad (7)$$

where ε denotes the carbon–carbon emissivity factor and is set to 0.9. T_{ref} is assumed to be equal to 300 K in this paper.

The ablative heat flux is formulated as follows:

$$\dot{q}_{ab} = \dot{m}_{ab}\left(h_w - h_u\right) \quad (8)$$

In Eq. [8], h_w and $\dot{m}_{ab}$ are calculated using the EST ablation model, and h_u is defined by:

$$h_u = \int_{T_{ref}}^{T_w} c_p \, dT \quad (9)$$

2.1 The EST Ablation Model

High temperatures and pressures within the boundary layer flow cause the chemical reactions between surface carbon and fluid dissociated components to be very fast and prevalent. This is a standard assumption in high temperature flows called chemical equilibrium. Figure 1 shows calculations for carbon ablation in air for two normalized freestream pressures. These graphs can be generated by both standard EST codes such as CEA or computational fluid dynamics (CFD) simulations of a reacting mixture. At temperatures between 1000 and 1500 K, finite rate oxidation reactions of carbonaceous materials take place. At 1500 to 3000 Kelvin, a plateau is observed in Fig. 1b due to the consumption of oxygen in the heterogeneous wall reactions, producing carbon monoxide. This is an exothermic reaction that lowers the wall enthalpy. At higher temperatures, the mass loss due to vaporization exceeds the diffusion-controlled oxidation mass loss rate. A sharp rise occurs in both graphs, expressing the occurrence of carbon sublimation and carbon–nitrogen formation which are endothermic in the overall energy change.

A kinetics expression for rate-controlled ablation, $\dot{m}_R$, can be combined with the above equilibrium calculations via
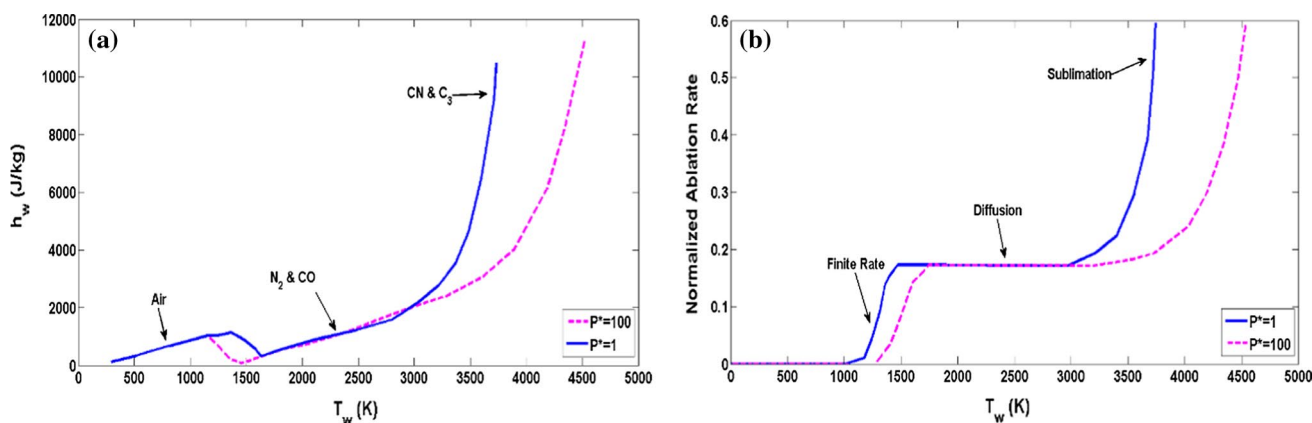
Fig. 1 EST ablation model of carbonaceous materials at two normalized pressures. **a** Wall enthalpy; **b** normalized ablation rate

Scala's second-order transition scheme to produce a general ablation rate which is as follows:

$$\frac{1}{\dot{m}_{ab}^2} = \frac{1}{\dot{m}_R^2} + \frac{1}{\dot{m}_{eq}^2} \tag{10}$$

where $\dot{m}_R$ is the rate-controlled oxidation of carbonaceous materials and is defined by:

$$\dot{m}_R = a_R \left(X_{O_2} P^*\right)^{0.5} \exp\left[-E_R / RT_w\right] \tag{11}$$

and $\dot{m}_{eq}$ is the equilibrium mass flux and is given by:

$$\dot{m}_{eq} = g_{h0}\, \phi_{blow,eq} \tag{12}$$

In Eq. [11], X_{O_2} is the mole fraction of oxygen in air (0.21), where a_R, E_R and R are reaction constants. For the sake of brevity, curve fittings of carbon–air EST calculation, introduced in [3], are not mentioned here and are all implemented in the solver.

2.2 Wall Recession and Grid Motion

Carbonaceous materials on the heated surface have recession due to the oxidation and sublimation in air. The amount of recession rate is computed as follows:

$$\dot{S}_w = \frac{\dot{m}_{ab}}{\rho_w} \tag{13}$$

where ρ_w is the heated wall density and is considered 1900 kg/m³ throughout this study.

3 Numerical Settings

A 5-centimeter semicircle nose is subjected to time-dependent flow conditions. The energy equation is solved with second-order upwind, and Green–Gauss cell-based gradient is utilized for spatial discretization. For time integration, a

second-order implicit transient formulation is applied with a time step size of 0.005 s. Thermal conductivity and specific heat of carbon–carbon material are assumed as linear and polynomial functions of the temperature, respectively. Due to the problem symmetry, a quarter of the circle is considered for simulation including arc line as the heated surface, the right side as the adiabatic wall and the bottom side as the symmetry line. Gambit, a preprocessor for FLUENT, is utilized to mesh the solid domain using triangular elements, refined close to the heated surface. Two grids are shown in Fig. 2. The left domain, called "base grid" in this study, contains 60 grid points along right and bottom sides of the domain and 100 points along the heated surface with 16,000 grid points. The right domain, called "fine grid," includes $100 \times 110 \times 200$ grid points along the boundaries, respectively, with an overall 26,000 grid points used for grid sensitivity study. The convergence criterion is set to 10^{-8} for energy equation residual [24].

The heated wall is subjected to a time-dependent heat flux based on cold wall where there is no ablation. An engineering correlation for stagnation point cold wall heating rate is adopted, i.e., $q_{cw} = 0.05 * \left(\rho_\infty / R_n\right)^{0.5} * u_\infty^3$. Time history of freestream density and velocity are $\rho_\infty = 1.75 t^*$ and $u_\infty = 6000 e^{-1.2t^*}$ where $t^* = e^{(t-30)/2.2}$, as shown in Fig. 3a, b. The recovery enthalpy is also assumed as the total enthalpy for the stagnation point, i.e., $h_r = u_\infty^2 / 2$. The freestream density rises by time which causes the stagnation point heat flux to increase. At $t = 25$th s, the maximum of stagnation cold wall heat flux is produced. Afterward, a decrement is observed in cold wall heat flux because of a significant decline in reentry vehicle (RV) velocity. A Newtonian blunt body assumption is regarded for pressure distribution, while cold wall heat flux and recovery enthalpy profiles are adopted to have cosine distribution over the arc, as shown in Fig. 3d. It is noteworthy that the employed cold wall heat flux used in this study can be easily replaced with the results of CFD simulations to account for real gas effects at cold

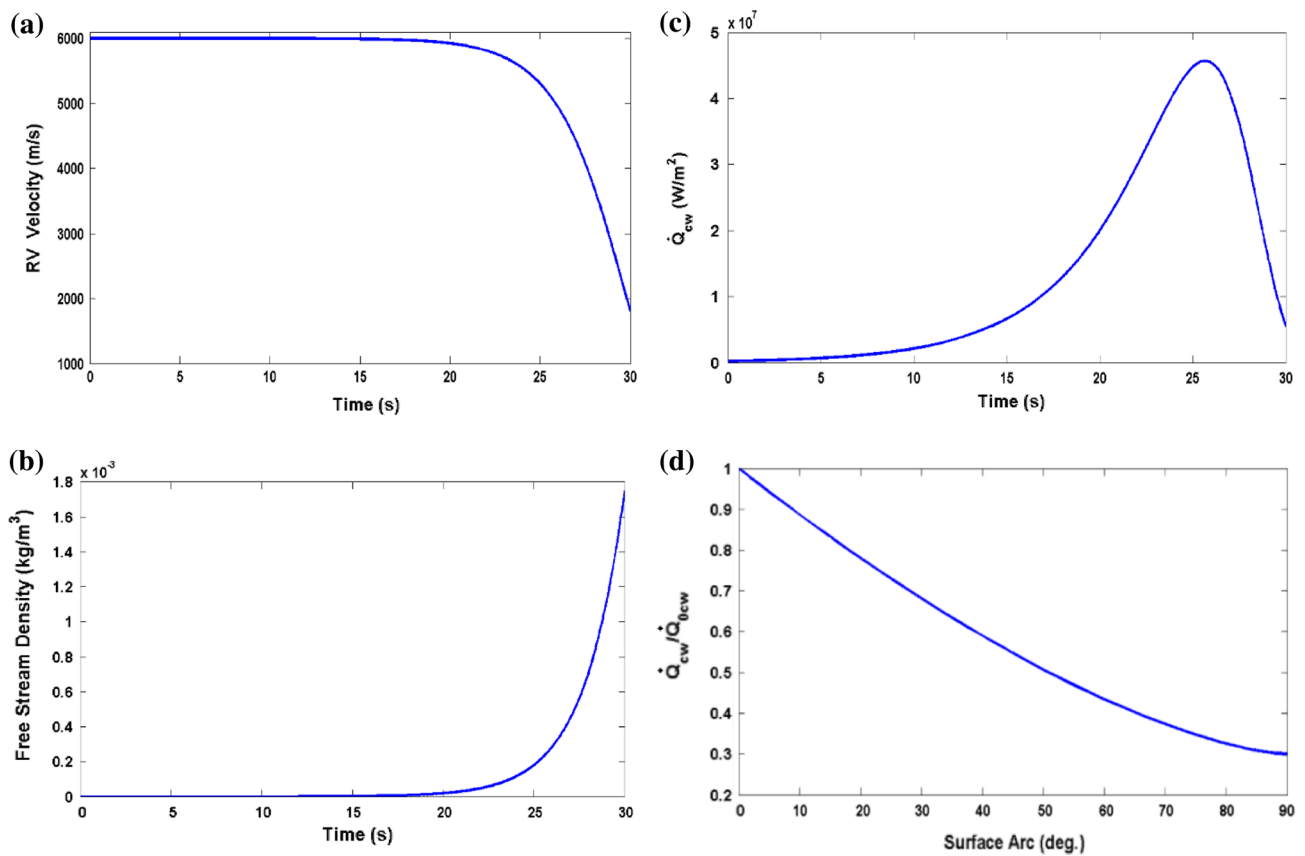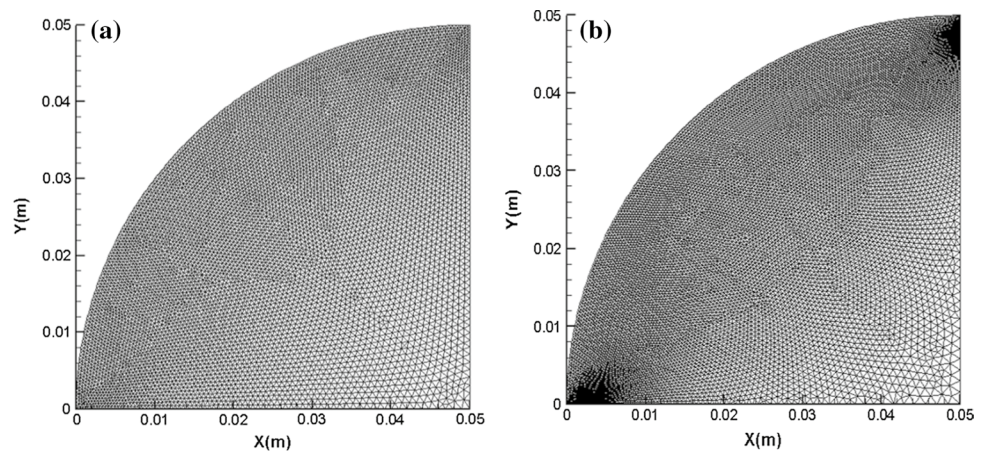**Fig. 2** Computational domain with two grid sizes. **a** Coarse grid; **b** fine grid

Fig. 3 Time histories of heated wall imposed conditions: **a** reentry velocity; **b** freestream density; **c** stagnation cold wall heat flux; **d** heat flux distribution over the heated wall

wall temperature. This is an alternative for highly coupled reacting flow field computations with one-dimensional thermal response codes conducted by some researchers which are time-consuming and have limited range of application along with convergence problems.

Different dynamic mesh techniques are available in FLUENT including layering [25], sliding [26], smoothing and remeshing [27]. In the current study, spring-based smoothing method is utilized in order to account for the grid motion caused by the heated wall recession. In this approach, the edges between any two mesh nodes are idealized as a network of interconnected springs. The initial spacing of the edges before any boundary motion constitutes the equilibrium state of the mesh. A displacement at a given boundary node will generate a force proportional to the displacement along all the springs connected to the node. The force on

a mesh node can be computed using the Hook's law [28]. Due to the small size of initial cells and the accumulation of deformation of ablative materials, a remeshing technique is also applied in order to avoid the occurrence of negative volumes, and consequently solution divergence. The recession of the heated wall cells is computed at each time step and is considered at normal direction of each cell.

4 Results and Discussions

4.1 The Isotropic Conductivity

In this section, the results of the implemented codes in the solver for isotropic conductivity are presented. Time history of stagnation point temperature response of current finite volume (F.V) analysis is compared with the available finite difference and HBI investigations in Fig. 4. The temperature gradually increases by time evolution up to $t = $10th s which is consistent with gentle rise of the cold wall heat flux

in Fig. 3c. Thereupon, the stagnation temperature response surges due to a sharp increase in the cold wall heat flux. As expected, the maximum temperature is computed at the relevant time of maximum cold wall heat flux and is in a good agreement with finite difference solutions. Moreover, the amount of temperature computed by current two-dimensional approach seems to be less than one-dimensional finite difference results up to $t = 18$th s. Besides, the amount of the maximum temperatures exceeds the diffusion phase of the ablation process of carbonaceous materials, according to Fig. 1 and falls in the sublimation region. Therefore, the formations of C_3 and CN are taken into account in this simulation.

Figure 5 illustrates the net heat flux imposed on the heated surface at the stagnation point. This flux is the summation of radiation, ablation and convection heat fluxes. The results of current F.V at the stagnation point agree well with the trend of finite difference computations. The HBI predictions, however, are in accordance with the outcomes of other methods up to $t = 15$th s. After this moment, discrepancy gets higher

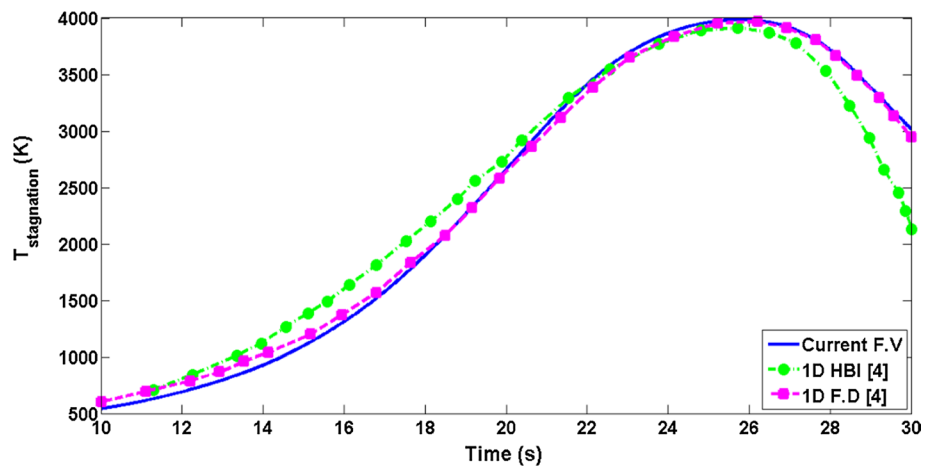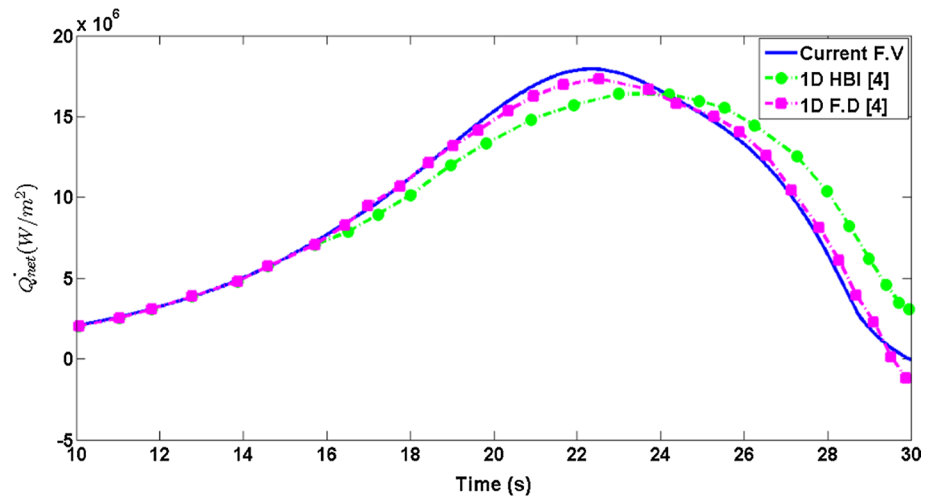**Fig. 4** Time history of the stagnation temperature

Fig. 5 Time history of the stagnation net heat flux

with a shift in time of the maximum value of the net flux. It is worth noting that at the final second of simulation, the value of the net heat flux becomes slightly negative in both current F.V study and the published finite difference outcomes in contrast to HBI predictions where this parameter must stay positive because of HBI formulation [4]. At this moment, the velocity of RV and consequently the recovery enthalpy are greatly reduced. The wall enthalpy, on the other hand, intensifies due to high amount of surface temperature, according to Fig. 1b. Thus, the difference between the recovery and wall enthalpies becomes negative which leads to negative values for the net flux, according to Eq. [3].

Figure 6 depicts time histories of convection, radiation and ablation heat fluxes averaged over the heated surface. Similarly, the final amounts of mean convection heat flux have become negative. Radiation heat flux behavior follows the wall temperature and achieves the maximum value when the wall temperature reaches the maximum magnitude. Therefore, the mean net heat flux also reaches negative values at the final seconds of simulation. It can be also seen

that the mean net heat flux maximizes sooner than the mean convection one, both earlier than the mean radiation counterpart. Up to $t = 17^{th}$ s, radiation flux is negligible compared to the convection, due to relatively low wall temperature which causes the net heat flux to be equal to the convection counterpart.

The variation of the averaged ablation heat flux over the heated surface is depicted in Fig. 7. Up to $t = 17$th s, the magnitude of wall temperature is about 1100 K and no surface reaction occurs. Thus, the mean ablation heat flux is almost zero. As the heated wall becomes hotter, the oxidation of carbonaceous surface starts with sublimation process to produce CO causing the wall enthalpy at the gas side, h_w, to decline between $t = 15$th s to $t = 17$th s. Afterward, h_w rises due to CN and C_3 formation up to $t = 26$ s, and then decreases following the surface temperature decline. However, the wall enthalpy at the underside, h_u, follows the surface temperature curve and is calculated according to Eq. [9]. The difference between these two enthalpies becomes negative expressing that

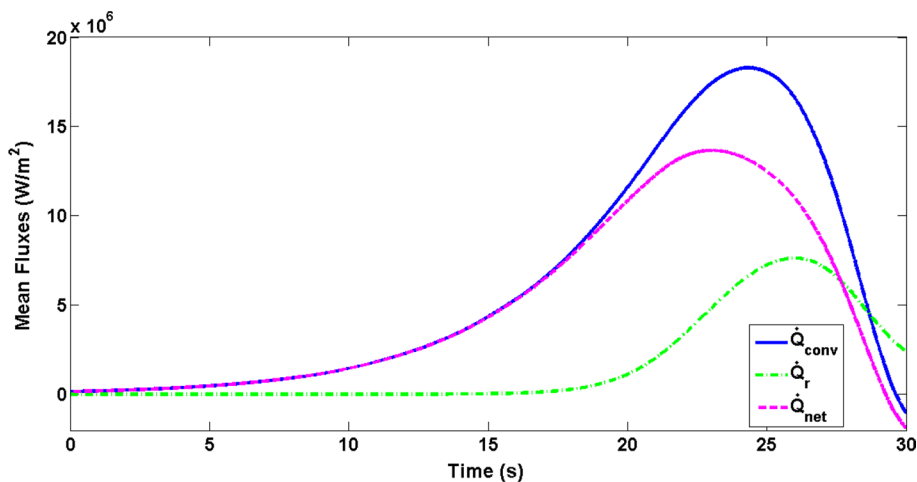**Fig. 6** Time histories of the mean heat fluxes

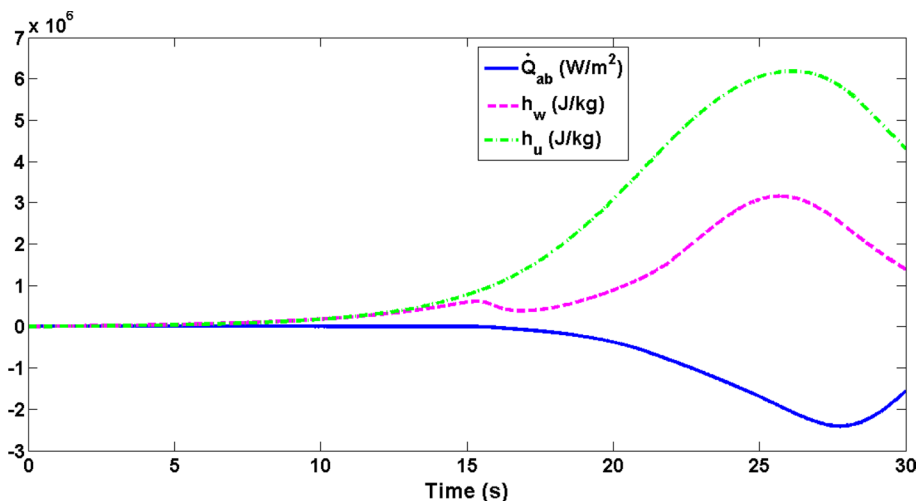**Fig. 7** Time history of the mean wall enthalpies and ablation heat flux

Fig. 8 Comparison of the stagnation point wall recession with the literature
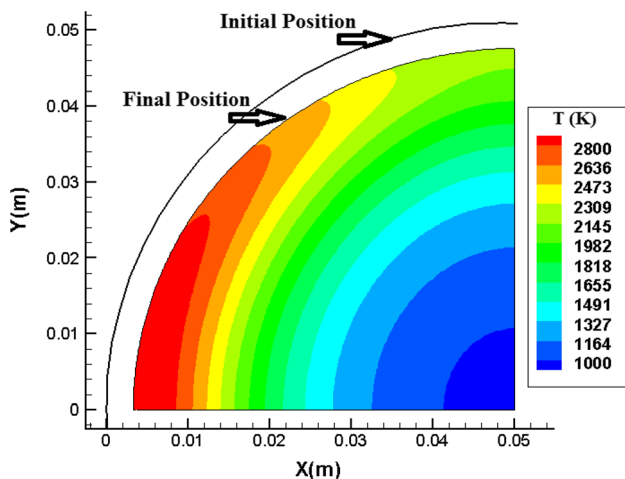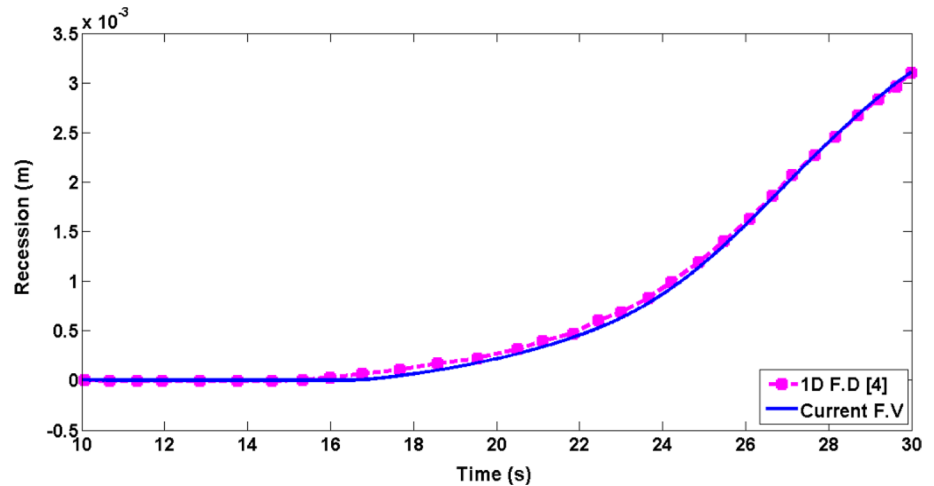

Fig. 9 Contour of the temperature field at $t = 30$th s

the carbon–carbon ablation heat flux slightly increases the net heat flux imposed to the heated wall. Nevertheless, ablation process generally reduces convection and the net heat flux via blowing the ablation products into the boundary layer.

Heated wall recession history at the stagnation point is shown in Fig. 8 and is compared with the finite difference results of the literature. As the ablation process starts, the heated surface recesses and its instantaneous magnitude is accumulated up to the final second, where almost 3 mm of the stagnation point is ablated and removed. This may lead to a non-negligible shape change of the stagnation point radius.

In Fig. 9, the contour of the temperature field of the recessed domain is revealed at the end of the simulation. Higher temperature is observed at areas near the stagnation point due to the greater amount of imposed heat flux. Two arrows can be seen in this figure indicating the initial and final arc positions. The surface ablation and

wall recession effects are evident. It is obvious that the amounts of ablation and surface removal are also greater near the stagnation point.

4.2 Grid Size and Time Step Studies

In Fig. 10, the results of stagnation point temperature and ablation mass flux are illustrated for two different grid size and time step in order to assure the independency of the simulation results. Figure 10a, b demonstrates the temperature and ablation mass flux for the base and fine grids. The comparison of the temperature and ablation mass for two integration time steps, i.e., 5×10^{-3} and 2.5×10^{-3} s is also shown in Fig. 10c, d. All these four graphs present almost identical results declaring both grid and time step insensitivity of the numerical solutions.

4.3 The Orthotropic Conductivity

Having validated the accuracy of the developed codes to simulate the ablation process, an investigation is conducted to study the thermal response behavior of the orthotropic conductivity in carbon–carbon in the following part. This can be considered as an application for multidimensional analysis of the ablation. The thermal conductivity tensor for an orthotropic material is defined by:

$$k_{ij} = \begin{bmatrix} k_{\text{TTT}} & 0 \\ 0 & k_{\text{IP}} \end{bmatrix} \tag{14}$$

Each component of this matrix is relevant to a principal orthogonal direction. Here, the material is assumed to be orthogonal. Considering the numerical domain in polar coordinate system, the radial direction is regarded as the "through-the-thickness" direction and the tangential plane is "in-plane" orientation. FLUENT computes
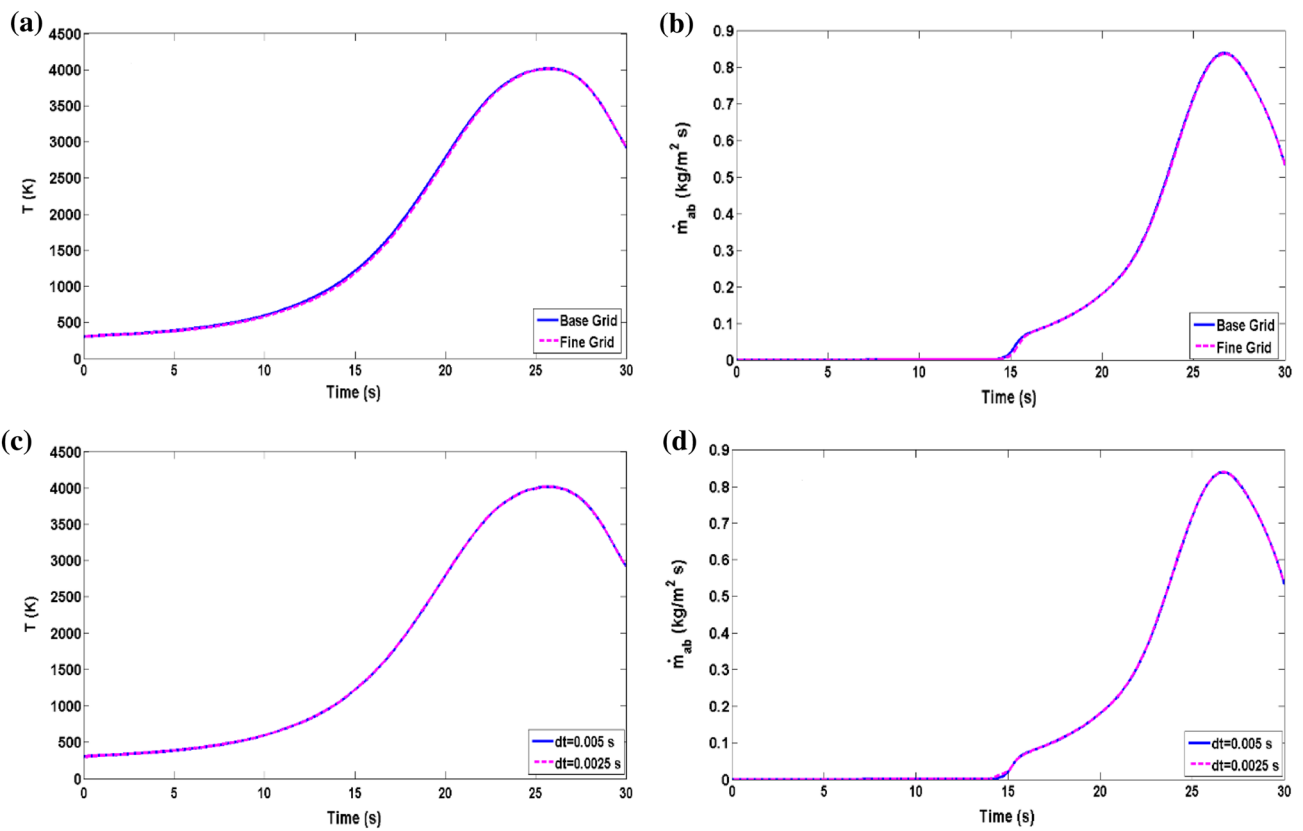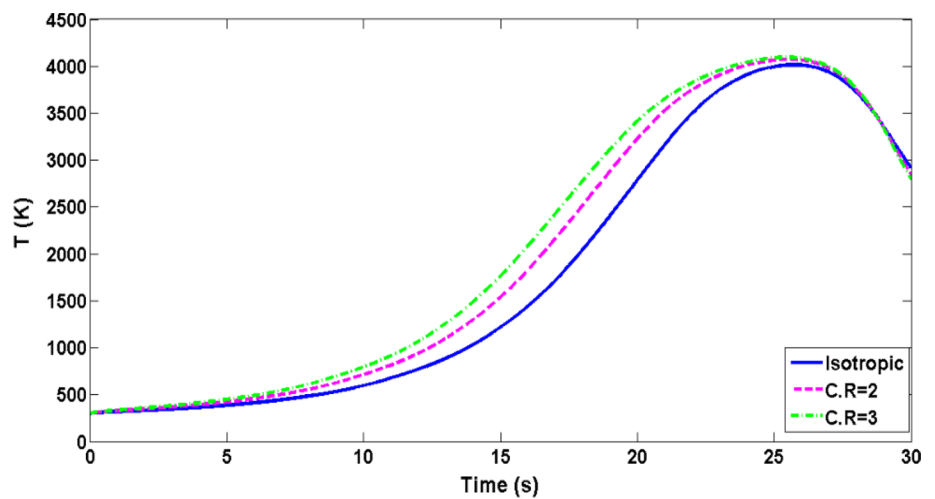
Fig. 10 Sensitivity analysis results. **a**, **b** Grid size; **c**, **d** time step size

Fig. 11 Effect of C.R on the stagnation temperature

the anisotropic conductivity matrix at each cell using the rotation matrix if these two conductivities along with the center of polar coordinate system are defined. The calculation is based on the location of each cell in the cylindrical coordinate system specified, as described in [28]. A parameter is defined as the ratio of the in-plane to through-the-thickness conductivities, i.e., C.R $= k_{IP}/k_{TTT}$.

Simulations are carried out for two C.R values, and the results are compared with the isotropic case. In orthotropic simulations, the in-plane conductivity is kept the same as the isotropic case and the through-the-thickness conductivity is decreased. In Fig. 11, the stagnation point temperature predictions for two C.R values compared with the isotropic case are presented. Increasing the C.R value

is equivalent to a decrease in k_{TTT}. Consequently, heat diffusivity in through-the thickness decreases which means lower heat conduction to backup structure. This leads to higher surface temperature in comparison with the isotropic case. However, this effect will become negligible as the stagnation temperature tends to 4000 K where the heat diffusion increases and the time lag in thermal response vanishes at the stagnation point.

Time variations of the stagnation point ablation mass flux for two orthotropic conductivities are compared with the isotropic case and shown in Fig. 12. Ablation process starts earlier along with higher maximum values as the amount of C.R increases due to the higher temperature rise caused by the lower heat diffusion in through-the-thickness direction. Nevertheless, the ablation mass flux is obtained identical for three case studies due to the similar temperature values at the final seconds of simulation.

Orthotropic conductivity influence on the stagnation convection heat flux is shown in Fig. 13. Based on Fig. 12, higher amount of ablation mass flux is obtained as the value of C.R increases. This injected gas into the

hot boundary layer imposes lower blowing factor which leads to a reduction in the convection heat flux, according to Eq. [4].

The influence of orthotropic conductivity on the net heat flux imposed on the heated surface is illustrated in Fig. 14. On the one hand, higher temperature and radiation heat flux are obtained by increasing the C.R value, according to Fig. 11. On the other hand, lower convection heat flux is achieved as the C.R value increases, based on Fig. 13. Although the magnitude of ablation heat flux increases by C.R increment as in Fig. 12 and it adds heat flux to the surface, the effects of convection heat flux reduction and radiation heat flux rise dominate the ablation heat flux impact. This yields an overall great decline in the net heat flux. In addition, the peak region of the graph becomes flatter as the value of C.R increases.

Eventually, the temperature field at different instances of time is illustrated for the isotropic and two orthotropic cases in Fig. 15. At each instant, there are higher temperatures near the heated surface and lower temperature toward the center of the circle as the C.R value increases. This is due to

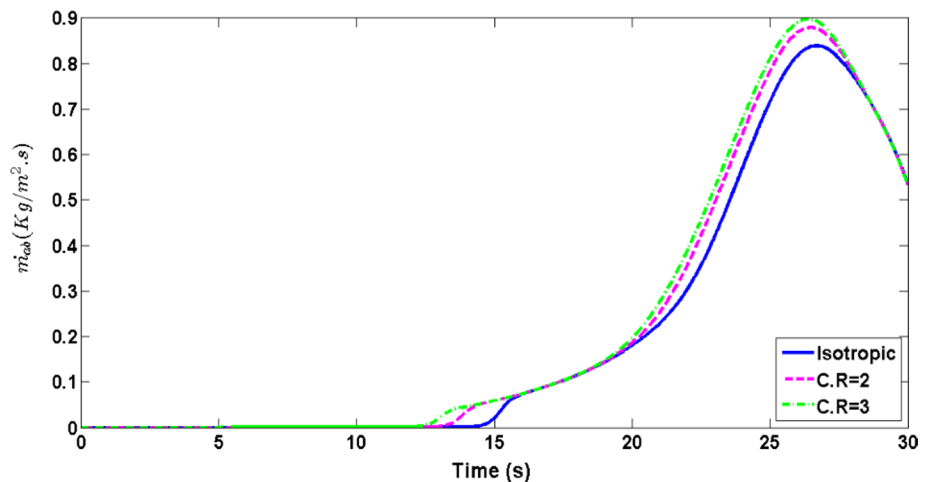**Fig. 12** Effect of C.R on the stagnation ablation mass flux

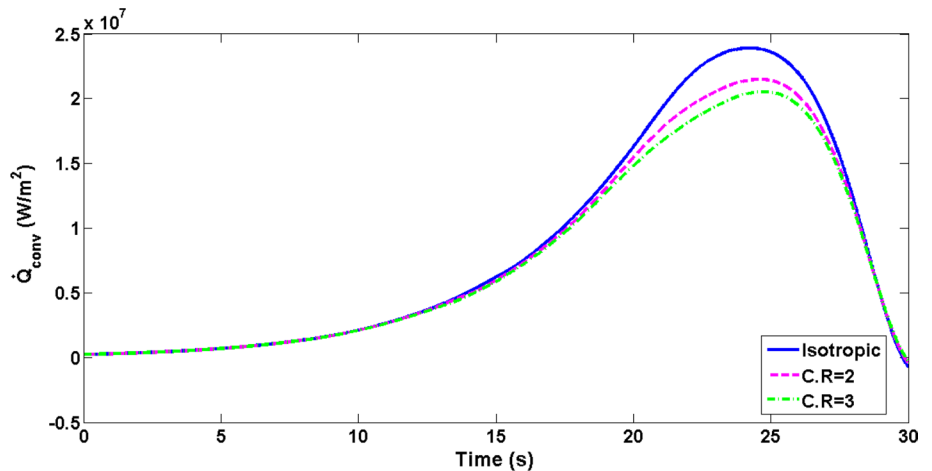**Fig. 13** Effect of C.R on the stagnation convection heat flux

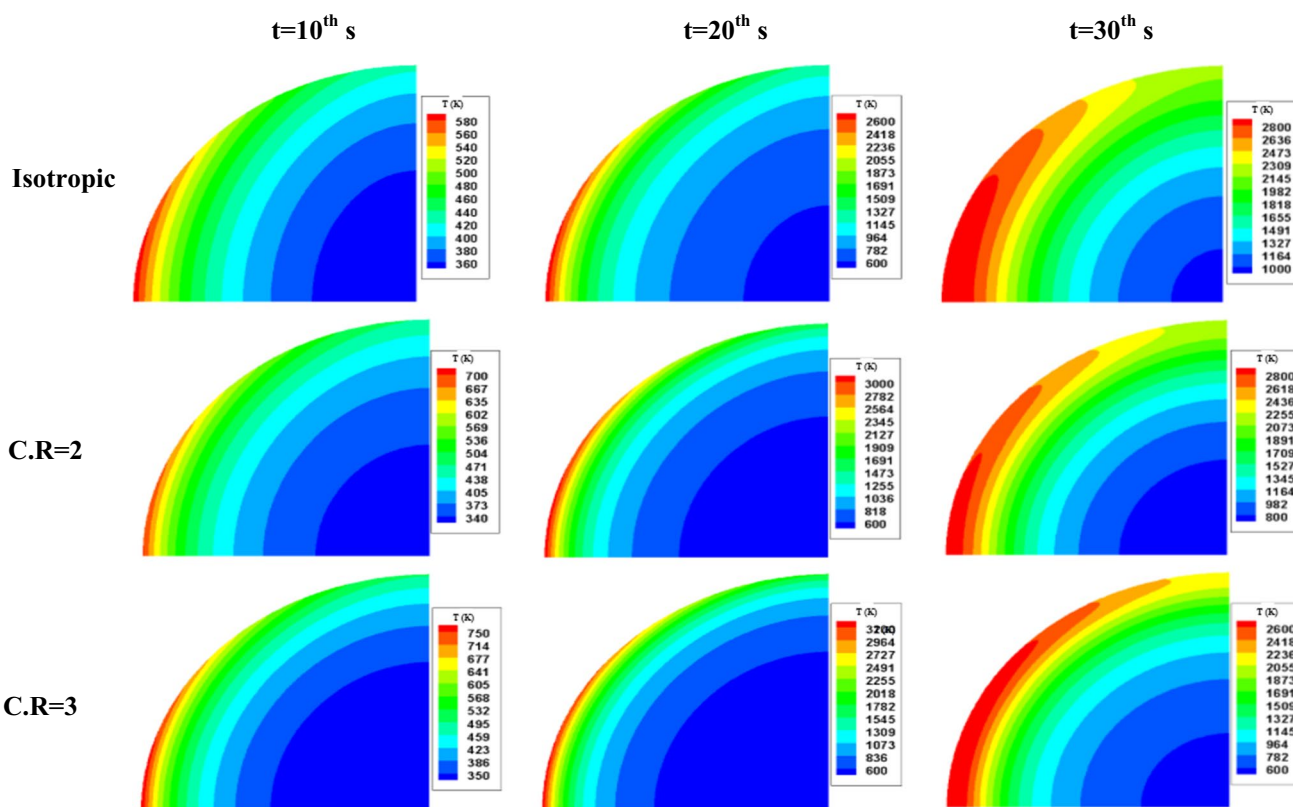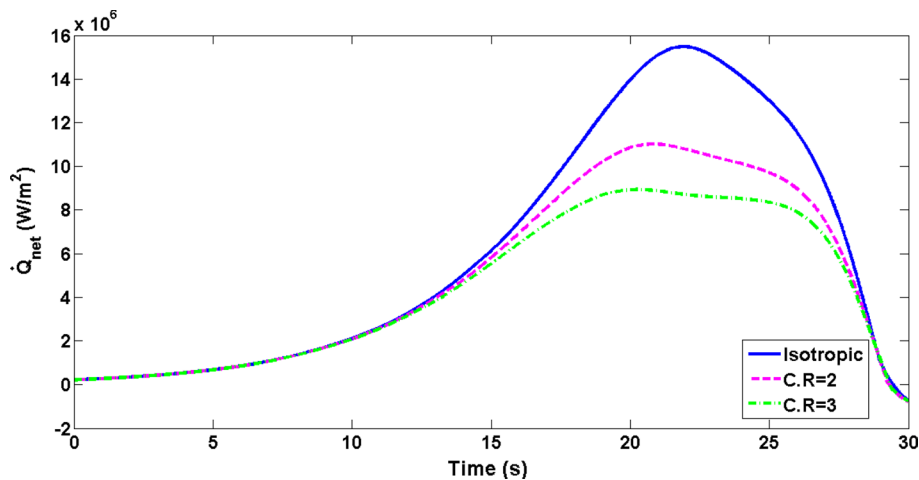**Fig. 14** Effect of C.R on the net heat flux

Fig. 15 Effect of C.R on the temperature field at various instances of time

modest amount of heat diffused to the interior region of the computational domain. In other words, less heat flux conducts through-the-thickness and more diffuses through the "in-plane" direction, keeping the core region of the circle at lower temperatures. Comparing the contours of temperature at $t = 30$th s for different C.R values, it is seen that an elongation of high-temperature zone in the azimuthal direction is generated near the heated surface.

5 Conclusion

In the first part of this study, the methodology of accurate multidimensional modeling of non-charring ablative materials in the commercial solver, FLUENT 6.3, was presented. Non-dimensional ablation mass flux, hot wall temperature and pressure-dependent behavior obtained from EST calculations along with the heated wall grid motion

were considered in the analysis via UDFs. A two-dimensional carbon–carbon isotropic material case study was thoroughly investigated, and the response of the stagnation point was compared with the one-dimensional finite difference and HBI results, and verified the developed codes and methodology. In the second part, the impacts of the orthotropic conductivity on thermal response of carbon–carbon were reported as well. Higher surface temperature, ablation mass flux and wall recession were achieved in the orthotropic case. Also, lower heat conducted toward the internal layers, and thus lower core region temperature was obtained by applying the orthotropic carbon–carbon material. These results were also acquired by increasing the "in-plane" to "through-the-thickness" conductivities ratio. In conclusion, this type of ablation modeling provides a fast multidimensional tool for thermal studies of non-charring heat shields in those applications where a one-dimensional finite difference approach is not able to accurately predict the thermal response such as sharp geometries or anisotropic materials. Moreover, the cold wall heat flux can be imported from CFD solutions of the flow field without direct coupling and possible numerical challenges. The computed temperature field can also be coupled with a structural solver to calculate the thermal stress for further multiphysics considerations.

Compliance with ethical standards

References

1. Mastanaiah, K.: Correlation of theoretical analysis with experimental data on the performance of charring ablators. J. Heat Transfer **98**(1), 139–143 (1976)
2. Blackwell, B.: Numerical prediction of one-dimensional ablation using a finite control volume procedure with exponential differencing. Numer. Heat Transf. Part A Appl. **14**(1), 17–34 (1988)
3. Potts, R.: Hybrid integral/quasi-steady solution of charring ablation. In: 5th Joint Thermophysics and Heat Transfer Conference 1990, p. 1677
4. Potts, R.L.: Application of integral methods to ablation charring erosion—a review. J. Spacecr. Rockets **32**(2), 200–209 (1995)
5. Candane, S.R.; Balaji, C.; Venkateshan, S.: Ablation and aerothermodynamic studies on thermal protection systems of sharp-nosed re-entry vehicles. J. Heat Transf. **129**(7), 912–916 (2007)
6. Chen, Y.; Delichatsios, M.; Motvalli, V.: Material pyrolysis properties, part I: an integral model for one-dimensional transient pyrolysis of charring and non-charring materials. Combust. Sci. Technol. **88**(5–6), 309–328 (1993)
7. Chen, Y.; Motevalli, V.; Delichatsios, M.: Material pyrolysis properties, part II: methodology for the derivation of pyrolysis properties for charring materials. Combust. Sci. Technol. **104**(4–6), 401–425 (1995)
8. Ruperti, N.J.; Cotta, R.M.; Falkenber, C.V.; Su, J.: Engineering analysis of ablative thermal protection for atmospheric reentry: improved lumped formulations and symbolic–numerical computation. Heat Transf. Eng. **25**(6), 101–111 (2004)
9. Amar, A.J.: Modeling of one-dimensional ablation with porous flow using finite control volume procedure. Master of Science Thesis, The Graduate Faculty, North Carolina State University (2006)
10. Candane, S.; Balaji, C.; Venkateshan, S.: A comparison of quasi one-dimensional and two-dimensional ablation models for subliming ablators. Heat Transf. Eng. **30**(3), 229–236 (2009)
11. Dec, J.A.: Three Dimensional Finite Element Ablative Thermal Response Analysis Applied To Heatshield Penetration Design. Georgia Institute of Technology, Atlanta (2010)
12. Arnas, A.Ö.; Boettner, D.D.; Tamm, G.; Norberg, S.A.; Whipple, J.R.; Benson, M.J.; VanPoppel, B.P.: On the analysis of the aerodynamic heating problem. J. Heat Transf. **132**(12), 124501 (2010)
13. Yang, L.; Zhang, Y.; Chen, J.: An integral approximate solution to ablation of a two-layer composite with a temporal Gaussian heat flux. Heat Transf. Eng. **32**(5), 418–428 (2011)
14. Ewing, M.E.; Laker, T.S.; Walker, D.T.: Numerical modeling of ablation heat transfer. J. Thermophys. Heat Transf. **27**(4), 615–632 (2013)
15. Martin, A.; Boyd, I.D.: Strongly coupled computation of material response and nonequilibrium flow for hypersonic ablation. J. Spacecr. Rockets **52**(1), 89–104 (2014)
16. Chen, Y.-K.; Gökçen, T.; Edquist, K.T.: Two-dimensional ablation and thermal response analyses for mars science laboratory heat shield. J. Spacecr. Rockets **52**(1), 134–143 (2014)
17. Qu, Z.; Li, W.; Zhang, J.; Tao, W.: Numerical study of heat conduction with a chemical reaction at the moving frontal surface for a graphite plate. Numer. Heat Transf. Part A Appl. **67**(2), 189–209 (2015)
18. Lachaud, J.; Aspa, Y.; Vignoles, G.: Analytical modeling of the transient ablation of a 3D C/C composite. Int. J. Heat Mass Transf. **115**, 1150–1165 (2017)
19. Wang, M.; Zhu, W.: Pore-scale study of heterogeneous chemical reaction for ablation of carbon fibers using the lattice Boltzmann method. Int. J. Heat Mass Transf. **126**, 1222–1239 (2018)
20. Zong, R.; Kang, R.; Hu, Y.; Zhi, Y.: Modeling the pyrolysis study of non-charring polymers under reduced pressure environments. Heat Mass Transf. **54**(4), 1135–1144 (2018)
21. Wang, J.; Wang, H.; Sun, J.; Wang, J.: Numerical simulation of control ablation by transpiration cooling. Heat Mass Transf. **43**(5), 471–478 (2007)
22. Qian, W.-Q.; He, K.-F.; Zhou, Y.: Estimation of surface heat flux for ablation and charring of thermal protection material. Heat Mass Transf. **52**(7), 1275–1281 (2016)
23. Putz, K.E.; Bartlett, E.P.: Heat-transfer and ablation-rate correlations for re-entry heat-shield and nosetip applications. J. Spacecr. Rockets **10**(1), 15–22 (1973)
24. Atmaca, M.; Girgin, I.; Ezgi, C.: CFD modeling of a diesel evaporator used in fuel cell systems. Int. J. Hydrog. Energy **41**(14), 6004–6012 (2016)
25. Firdaus, S.; Abdullah, M.; Abdullah, M.; Fairuz, Z.: Heat transfer performance of a synthetic jet at various driving frequencies and diaphragm amplitude. Arab. J. Sci. Eng. **44**(2), 1043–1055 (2019)
26. Atmaca, M.; Çetin, B., Yılmaz, E.: CFD analysis of unmanned aerial vehicles (UAV) moving in flocks. Acta Phys. Pol. A. **135**(4), 694 (2019). https://doi.org/10.12693/APhysPolA.135.694
27. Shao, W.; Cui, Z.; Wang, N.; Cheng, L.: Numerical simulation of heat transfer process in cement grate cooler based on dynamic mesh technique. Sci. China Technol. Sci. **59**(7), 1065–1070 (2016)
28. Fluent, F.: 6.3 User's Guide. Fluent Inc, New York (2006)